Wave Motion 106 (2021) 102793

Contents lists available at ScienceDirect

Wave Motion

journal homepage: www.elsevier.com/locate/wamot

Numerical bifurcation and stability for the capillary–gravity Whitham equation

Efstathios G. Charalampidis [a,*], Vera Mikyoung Hur [b,1]

[a] Mathematics Department, California Polytechnic State University San Luis Obispo, CA 93407-0403, USA
[b] Department of Mathematics, University of Illinois at Urbana-Champaign Urbana, IL 61801, USA

ARTICLE INFO

Article history:
Received 3 February 2021
Received in revised form 22 June 2021
Accepted 24 June 2021
Available online 30 June 2021

Keywords:
Capillary-gravity Whitham equation
Periodic travelling waves
Global bifurcation
Orbital stability

ABSTRACT

We adopt a robust numerical continuation scheme to examine the global bifurcation of periodic travelling waves of the capillary–gravity Whitham equation, which combines the dispersion in the linear theory of capillary–gravity waves and a shallow water nonlinearity. We employ a highly accurate numerical method for space discretization and time stepping, to address orbital stability and instability for a rich variety of the solutions. Our findings can help classify capillary–gravity waves and understand their long-term dynamics.

1. Introduction

Whitham in his 1967 paper [1] (see also [2]) put forward

$$u_t + c_{\mathrm{ww}}(|\partial_x|)u_x + \frac{3}{2}\sqrt{\frac{g}{h}}uu_x = 0 \tag{1}$$

to address, qualitatively, breaking and peaking of waves in shallow water. Here and throughout, $u(x,t)$ is related to the displacement of the fluid surface from the rest state at position x and time t, and $c_{\mathrm{ww}}(|\partial_x|)$ is a Fourier multiplier operator, defined as

$$\widehat{c_{\mathrm{ww}}(|\partial_x|)f}(k) = \sqrt{\frac{g\tanh(kh)}{k}}\,\widehat{f}(k), \tag{2}$$

where g is the gravitational constant and h the undisturbed fluid depth. We remark that $c_{\mathrm{ww}}(k)$ is the phase speed of $2\pi/k$ periodic waves in the linear theory of water waves [2].

For relatively shallow water or, equivalently, relatively long waves such that $kh \ll 1$, one can expand the right hand side of (2) to obtain

$$c_{\mathrm{ww}}(k) = \sqrt{gh}\left(1 - \frac{1}{6}k^2h^2\right) + O(k^4h^4),$$

* Corresponding author.
E-mail addresses: echarala@calpoly.edu (E.G. Charalampidis), verahur@math.uiuc.edu (V.M. Hur).

[1] VMH is supported by the National Science Foundation through DMS-2009981.

https://doi.org/10.1016/j.wavemoti.2021.102793

whereby arriving at the celebrated Korteweg–de Vries (KdV) equation:

$$u_t + \sqrt{gh}\Big(u_x + \frac{1}{6}h^2 u_{xxx}\Big) + \frac{3}{2}\sqrt{\frac{g}{h}}uu_x = 0. \tag{3}$$

Therefore (1) and (2) can be regarded as augmenting (3) to include the *full* dispersion in the linear theory of water waves and, thus, improving over (3) for short and intermediately long waves. Indeed, numerical studies (see [3], for instance) reveal that the Whitham equation performs on par with or better than the KdV equation and other shallow water models in a wide range of amplitude and wavelength parameters.

The KdV equation admits solitary and cnoidal waves but no travelling waves can 'peak'. By contrast, the so-called extreme Stokes wave possesses a 120° peaking at the crest. Also no solutions of (3) can 'break'. That means, the solution remains bounded but its slope becomes unbounded. See [2, Section 13.14] for more discussion. This is perhaps not surprising because the dispersion[2] of the KdV equation is inadequate for explaining high frequency phenomena of water waves. Whitham [1,2] conjectured breaking and peaking for (1) and (2). Recently, one of the authors [4] proved breaking, and Ehrnström and Wahlén [5] proved peaking. Johnson and one of the authors [6] proved that a small amplitude and periodic travelling wave of (1) and (2) is modulationally unstable, provided that $kh > 1.145\ldots$, comparing with the well-known Benjamin–Feir instability of a Stokes wave. By contrast, all cnoidal waves of (3) are modulationally stable.

When the effects of surface tension are included, Johnson and one of the authors [7] proposed to replace (2) by

$$\widehat{c_{\mathrm{ww}}(|\partial_x|;T)f}(k) = \sqrt{(g+Tk^2)\frac{\tanh(kh)}{k}}\,\widehat{f}(k), \tag{4}$$

where T is the surface tension coefficient. We remark that $c_{\mathrm{ww}}(k;T)$ is the phase speed in the linear theory of capillary–gravity waves [2]. When $T = 0$, (4) becomes (2). Notice

$$c_{\mathrm{ww}}(k;T) = \sqrt{gh}\Big(1 - \frac{1}{2}\Big(\frac{1}{3} - \frac{T}{gh^2}\Big)k^2h^2\Big) + O(k^4h^4) \quad \text{as } kh \to 0,$$

and one arrives at the KdV equation for capillary–gravity waves:

$$u_t + \sqrt{gh}\Big(u_x + \frac{1}{2}\Big(\frac{1}{3} - \frac{T}{gh^2}\Big)h^2u_{xxx}\Big) + \frac{3}{2}\sqrt{\frac{g}{h}}uu_x = 0 \tag{5}$$

in the long wavelength limit unless $T/gh^2 = 1/3$. Notice that (3) and (5) behave alike, qualitatively, possibly after a sign change. By contrast, whenever $T > 0$, $c_{\mathrm{ww}}(k;T) \to \sqrt{T|k|}$ as $kh \to \infty$, whereby (1) and (4) become

$$u_t + \sqrt{T}|\partial_x|^{1/2}u_x + \frac{3}{2}\sqrt{\frac{g}{h}}uu_x = 0 \tag{6}$$

to leading order whereas when $T = 0$, $u_t + \sqrt{g}|\partial_x|^{-1/2}u_x + \frac{3}{2}\sqrt{\frac{g}{h}}uu_x = 0$.

In recent years, the *capillary–gravity Whitham equation* has been a subject of active research [7–11] (see also [12–16]). Particularly, Remonato and Kalisch [8] combined a spectral collocation method and a numerical continuation approach to discover a rich variety of local bifurcation of periodic travelling waves of (1) and (4), notably, crossing and connecting solution branches. Here we adopt a robust numerical continuation scheme to corroborate the results and produce convincing results for global bifurcation. Our findings support local bifurcation theorems (see [11], for instance) and help classify *all* periodic travelling waves.

We employ an efficient numerical method for solving stiff nonlinear PDEs implemented with fourth-order time differencing, to experiment with (nonlinear) orbital stability and instability for a plethora of periodic travelling waves of (1) and (4). Spectral modulational stability and instability were investigated numerically [10] and also analytically for small amplitude [7]. To the best of the authors' knowledge, however, nonlinear stability and instability have not been addressed. Our novel findings include, among many others, orbital stability for the $k = 1$ branch whenever $T > 0$ versus instability for the $k \geqslant 2, \in \mathbb{N}$ branches for great wave height when $0 < T/gh^2 \leqslant 1/3$.

The methodology here is potentially useful for tackling the capillary–gravity wave problem and other nonlinear dispersive equations.

2. Preliminaries

We rewrite (1) and (4) succinctly as

$$u_t + c_{\mathrm{ww}}(|\partial_x|;T)u_x + (u^2)_x = 0, \quad \text{where} \quad \widehat{c_{\mathrm{ww}}(|\partial_x|;T)f}(k) = \sqrt{(1+Tk^2)\frac{\tanh(k)}{k}}\,\widehat{f}(k). \tag{7}$$

[2] The phase speed is $\sqrt{gh}(1 - \frac{1}{6}k^2h^2)$, poorly approximating $c_{\mathrm{ww}}(k)$ when $kh \gg 1$.

Seeking a periodic travelling wave of (7), let

$$u(x,t) = \phi(z), \quad z = k(x - ct),$$

where $c \neq 0, \in \mathbb{R}$ is the wave speed, $k > 0$ the wave number, and ϕ satisfies by quadrature and Galilean invariance

$$-c\phi + c_{\mathrm{ww}}(k|\partial_z|;T)\phi + \phi^2 = 0. \tag{8}$$

We assume that ϕ is 2π periodic and even in the z variable, so that $2\pi/k$ periodic in the x variable. Notice

$$c_{\mathrm{ww}}(k|\partial_z|;T)\begin{Bmatrix}\cos\\ \sin\end{Bmatrix}(nz) = c_{\mathrm{ww}}(kn;T)\begin{Bmatrix}\cos\\ \sin\end{Bmatrix}(nz), \quad n \in \mathbb{Z}. \tag{9}$$

For any $T \geqslant 0$, $k > 0$ and $c \in \mathbb{R}$, clearly, $\phi(z) = 0$ solves (8) and (9). Suppose that T and k are fixed. A necessary condition for nontrivial solutions to bifurcate from such trivial solution at some c is that

$$c_{\mathrm{ww}}(k|\partial_z|;T)\phi - c\phi = 0 \text{ admits a nontrivial solution,}$$

if and only if $c = c_{\mathrm{ww}}(kn;T)$ for some $n \in \mathbb{N}$, by symmetry, so that

$$\cos(nz) \in \ker(c_{\mathrm{ww}}(k|\partial_z|;T) - c_{\mathrm{ww}}(kn;T)) \text{ in some space of even functions.}$$

When $T = 0$, $c_{\mathrm{ww}}(\cdot\,;0)$ monotonically decreases to zero over $(0,\infty)$, whence for any $k > 0$, $c_{\mathrm{ww}}(kn_1;T) > c_{\mathrm{ww}}(kn_2;T)$ whenever $n_1, n_2 \in \mathbb{N}$ and $n_1 > n_2$. Therefore, for any $k > 0$ for any $n \in \mathbb{N}$, $\ker(c_{\mathrm{ww}}(k|\partial_z|;0) - c_{\mathrm{ww}}(kn;0)) = \mathrm{span}\{\cos(nz)\}$ in spaces of even functions.

When $T \geqslant 1/3$, $c_{\mathrm{ww}}(\cdot\,;T)$ monotonically increases over $(0,\infty)$ and unbounded from above, so that for any $k > 0$ for any $n \in \mathbb{N}$, $\ker(c_{\mathrm{ww}}(k|\partial_z|;T) - c_{\mathrm{ww}}(kn;T)) = \mathrm{span}\{\cos(nz)\}$.

When $T < 1/3$, on the other hand, $c_{\mathrm{ww}}(kn_1;T) = c_{\mathrm{ww}}(kn_2;T)$ for some $k > 0$ for some $n_1, n_2 \in \mathbb{N}$ and $n_1 \neq n_2$ provided that $T = T(kn_1, kn_2)$, where

$$T(kn_1, kn_2) = \frac{1}{kn_1}\frac{1}{kn_2}\frac{n_1\tanh(kn_2) - n_2\tanh(kn_1)}{n_1\tanh(kn_1) - n_2\tanh(kn_2)}, \tag{10}$$

so that $\ker(c_{\mathrm{ww}}(k|\partial_z|;T) - c) = \mathrm{span}\{\cos(n_1 z), \cos(n_2 z)\}$, where $c = c_{\mathrm{ww}}(kn_1;T) = c_{\mathrm{ww}}(kn_2;T)$; otherwise, $\ker(c_{\mathrm{ww}}(k|\partial_z|;T) - c_{\mathrm{ww}}(kn;T)) = \mathrm{span}\{\cos(nz)\}$.

Suppose that $T \geqslant 0$, $k > 0$, and $T \neq T(kn, kn')$ for any $n, n' \in \mathbb{N}$ and $n \neq n'$, particularly, either $T = 0$ or $T \geqslant 1/3$. We assume without loss of generality $n = 1$. There exists a one-parameter curve of nontrivial, 2π periodic and even solutions of (8) and (9), denoted by

$$(\phi(z;s), c(s)), \quad |s| \ll 1, \tag{11}$$

in some function space (see, for instance, [5,11] for details), and

$$\begin{aligned}\phi(z;s) &= s\cos(z) + \frac{s^2}{2}\left(\frac{1}{c_{\mathrm{ww}}(k;T) - c_{\mathrm{ww}}(0;T)} - \frac{1}{c_{\mathrm{ww}}(k;T) - c_{\mathrm{ww}}(2k;T)}\cos(2z)\right)\\ &\quad + \frac{s^3}{2}\frac{1}{(c_{\mathrm{ww}}(k;T) - c_{\mathrm{ww}}(2k;T))(c_{\mathrm{ww}}(k;T) - c_{\mathrm{ww}}(3k;T))}\cos(3z) + O(s^4),\\ c(s) &= c_{\mathrm{ww}}(k;T) + s^2\left(\frac{1}{c_{\mathrm{ww}}(k;T) - c_{\mathrm{ww}}(0;T)} - \frac{1}{2}\frac{1}{c_{\mathrm{ww}}(k;T) - c_{\mathrm{ww}}(2k;T)}\right) + O(s^4)\end{aligned} \tag{12}$$

as $|s| \to 0$. Moreover, subject to a 'bifurcation condition' (see, for instance, [5,11] for details), (11) extends to all $s \in [0,\infty)$. See [5,11] and references therein for a rigorous proof.

When $T = 0$ and, without loss of generality, $k = 1$, $(\phi(z;s_j), c(s_j)) \to (\phi(z), c)$ as $j \to \infty$ for some $s_j \to \infty$ as $j \to \infty$ for some $\phi \in C^{1/2}([-\pi,\pi]) \bigcap C^\infty([-\pi,0) \bigcup (0,\pi])$ and $c \in (0,\infty)$ such that

$$\phi(0) = \frac{c}{2}. \tag{13}$$

See [5] and references therein for a rigorous proof. Indeed, such a limiting solution enjoys $\phi(z) \sim \frac{c}{2} - \sqrt{\frac{\pi}{8}}|z|^{1/2}$ as $|z| \to 0$.

When $T \geqslant 4/\pi^2$, for which the Fourier transform of $c_{\mathrm{ww}}(k|\partial_z|;T)^{-1}$ is 'completely monotone' [11], and $k = 1$, on the other hand,

$\|(\phi(\cdot;s), c(s))\| \to \infty$ as $s \to \infty$ in some[3] function space, or
$(\phi(z;s), c(s))$ is periodic in the s variable.

[3] A Hölder–Zygmund space, for instance [11]

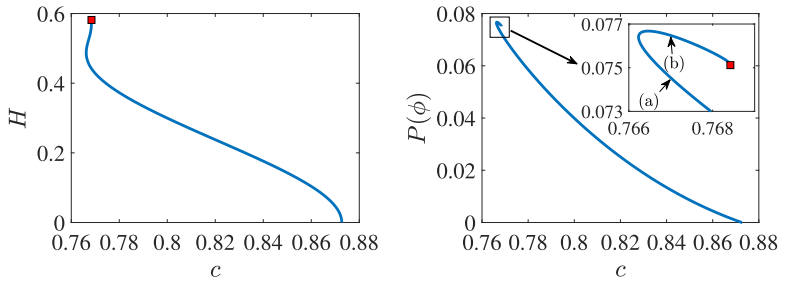

Fig. 1. $T = 0$, $k = 1$. Wave height (left, see (24)) and momentum (right, see (25)) vs. wave speed. The red square corresponds to the limiting solution (see (13)), for which $c \approx 0.76842127$. See Fig. 2 for the profiles at the points labelled with (a) and (b) in the inset of the right panel.

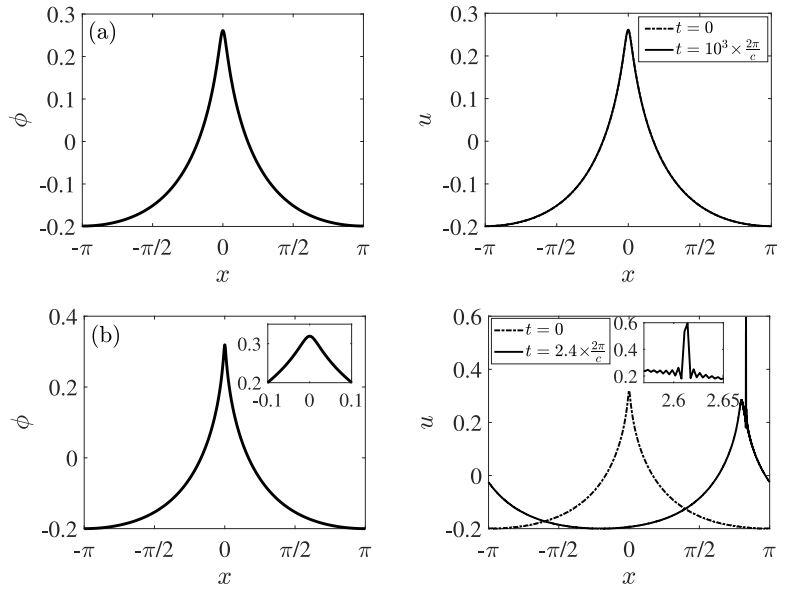

Fig. 2. $T = 0$, $k = 1$. Left column: almost limiting waves at the points labelled with (a) and (b) in the inset of the right panel of Fig. 1, prior to (a) and past (b) the turning point of P, for which $c = 0.767$. Right column: profiles perturbed by uniform random distributions of amplitudes $10^{-3} \times \|\phi\|_{L^\infty}$ at $t = 0$ (dash-dotted), and of the solutions of (7) at later instants of time (solid, see the legends), after translation of the x axis (a). The insets in the bottom panels are close-ups near the crests.

See [11], for instance, for a rigorous proof. Our numerical findings suggest $\min_{z\in[-\pi,\pi]} \phi(z;s) \to -\infty$ as $s \to \infty$. But such a limiting scenario would be physically unrealistic because the capillary–gravity Whitham equation models water waves in the finite depth. We say that a 2π periodic solution of (8) and (9) is admissible if

$$\phi(z) - \frac{1}{2\pi}\int_{-\pi}^{\pi} \phi(z)\, dz > -1 \quad \text{for all } z \in [-\pi, \pi],$$

implying that the fluid surface does not intersect the impermeable bed, and we stop numerical continuation once we reach a *limiting admissible solution*, which satisfies

$$\min_{z\in[-\pi,\pi]} \phi(z) - \frac{1}{2\pi}\int_{-\pi}^{\pi} \phi(z)\, dz = -1. \tag{14}$$

Section 4 provides examples.

Suppose on the other hand that $T = T(kn_1, kn_2)$ (see (10)) for some $k > 0$ for some $n_1, n_2 \in \mathbb{N}$ and $n_1 < n_2$, so that $c_{\mathrm{ww}}(kn_1; T) = c_{\mathrm{ww}}(kn_2; T) =: c$. Suppose that n_1 does not divide n_2. There exists a two-parameter sheet of nontrivial, periodic and even solutions of (8) and (9), and

$$\begin{aligned} &\phi(z; s_1, s_2) = s_1 \cos(n_1 z) + s_2 \cos(n_2 z) + O((|s_1| + |s_2|)^2), \\ &c(s_1, s_2) = c + O((|s_1| + |s_2|)^2), \\ &k(s_1, s_2) = k + O((|s_1| + |s_2|)^2) \end{aligned} \tag{15}$$

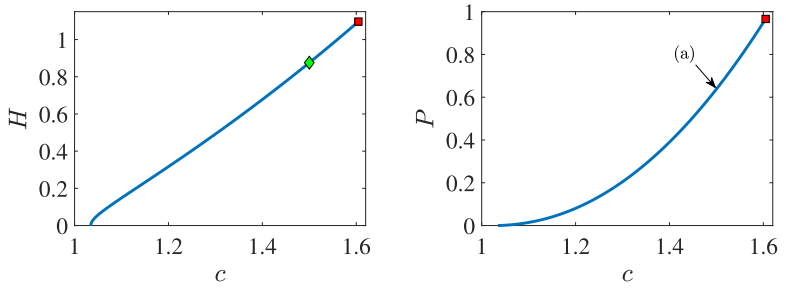

Fig. 3. $T = 4/\pi^2$, $k = 1$. H (left) and P (right) vs. c. The red square corresponds to the limiting admissible solution (see (14)), for which $c \approx 1.6047287696$. See Fig. 4 for the profile at the point labelled with (a) (the wave height is marked by a green diamond in the left panel).

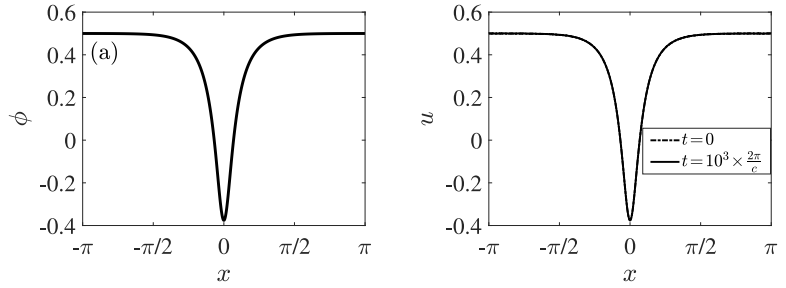

Fig. 4. $T = 4/\pi^2$, $k = 1$. On the left, the profile at the point labelled with (a) in Fig. 3, for which $c = 1.5$, and on the right, the profiles perturbed by uniformly distributed random noise of amplitude $10^{-3} \times \|\phi\|_{L^\infty}$ at $t = 0$ (dash-dotted) and of the solution of (7) at $t = 10^3 \times 2\pi/c$ (solid), after translation of the x axis.

for $|s_1|, |s_2| \ll 1$. We emphasize that k is a bifurcation parameter. Otherwise, n_1 divides n_2, and (15) holds for $|s_1|, |s_2| \ll 1$ and $s_2 > s_0 > 0$ for some s_0. In other words, there cannot exist $2\pi/n_1$ periodic and 'unimodal' waves, whose profile monotonically decreases from a single crest to the trough over the period. See [11], for instance, for a rigorous proof. See also [17–19] and others for capillary–gravity waves. The global continuation of (15) and limiting configurations have not been well understood analytically, though, and here we address numerically.

Turning the attention to the (nonlinear) orbital stability and instability of a periodic travelling wave of (7), notice that (7) possesses three conservation laws:

$$\begin{aligned} E(u) &= \int \left(\frac{1}{2} u c_{\mathrm{ww}}(|\partial_x|; T) u + \frac{1}{3} u^3 \right) dx, \\ P(u) &= \int \frac{1}{2} u^2 \, dx, \\ M(u) &= \int u \, dx, \end{aligned} \tag{16}$$

and so does the KdV equation with fractional dispersion:

$$u_t + |\partial_x|^\alpha u_x + (u^2)_x = 0, \quad 0 < \alpha \leqslant 2, \quad \text{where} \quad \widehat{|\partial_x|^\alpha f}(k) = |k|^\alpha \widehat{f}(k), \tag{17}$$

for which $E(u) = \int (\frac{1}{2} u |\partial_x|^\alpha u + \frac{1}{3} u^3) \, dx$ rather than the first equation of (16). We pause to remark that (7) becomes (17), $\alpha = 1/2$, for high frequency (see (6)), and (3) and (5) compare with $\alpha = 2$. A solitary wave of (17) is a minimizer of E subject to that P is constant, and orbitally stable provided that $P_c > 0$ if and only if $\alpha > 1/2$. See [20] and references therein for a rigorous proof. See also [21] for an analogous result for periodic travelling waves. It seems not unreasonable to expect that the orbital stability and instability of a periodic travelling wave of (7) change likewise at a critical point of P as a function of c although there is no rigorous analysis of constrained minimization to the best of the authors' knowledge. Indeed, numerical evidence [22] supports the conjecture when $T = 0$ and $k = 1$. Here we take matters further to $T \geqslant 0$ and $k \geqslant 1, \in \mathbb{N}$. Also we numerically elucidate the instability scenario when $T = 0$ and $k = 1$.

3. Methodology

We begin by numerically approximating 2π periodic and even solutions of (8) and (9) by means of a spectral collocation method [23,24]. See [22], among others, for nonlinear dispersive equations of the form (7) and (17). We define the

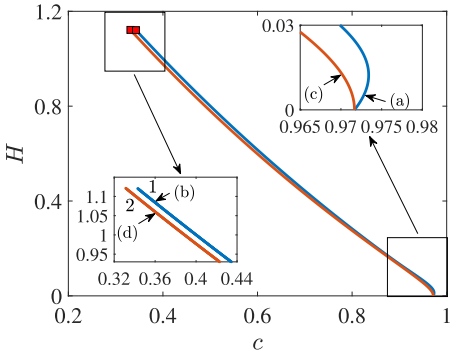

Fig. 5. $T = T(1, 2)$ (see (10)). H vs. c for $k = 1$ (blue) and $k = 2$ (orange). The red squares correspond to the limiting admissible solutions for the $k = 1$ and $k = 2$ branches, for which $c \approx 0.3429722287$ and $c \approx 0.33120532402$, respectively. Insets are close-ups near the beginning and end of numerical continuations. See Fig. 6 for the profiles at the points labelled with (a) through (d) in the insets. (For interpretation of the references to colour in this figure legend, the reader is referred to the web version of this article.)

collocation projection as a discrete cosine transform as

$$\phi_N(z) = \sum_{n=0}^{N-1} \omega(n)\widehat{\phi}(n)\cos(nz), \tag{18}$$

where the discrete cosine coefficients are

$$\widehat{\phi}(n) = \omega(n)\sum_{m=1}^{N} \phi_N(z_m)\cos(nz_m) \tag{19}$$

and

$$\omega(n) = \begin{cases} \sqrt{1/N} & \text{for } n = 0, \\ \sqrt{2/N} & \text{otherwise,} \end{cases}$$

the collocation points are

$$z_m = \pi\frac{2m-1}{2N}, \quad m = 1, 2, \ldots, N.$$

Therefore

$$\phi(z) \approx \phi_N(z) = \sum_{m=1}^{N}\sum_{n=0}^{N-1} \omega^2(n)\cos(nz_m)\cos(nz)\phi(z_m).$$

We can compute (18) and (19) efficiently using a fast Fourier transform (FFT) [24]. For $T \geqslant 0$ and $k > 0$, likewise,

$$c_{\mathrm{ww}}(k|\partial_z|; T)\phi(z) \approx (c_{\mathrm{ww}}(k|\partial_z|; T)\phi)_N(z) := \sum_{\ell=1}^{N}\sum_{n=0}^{N-1} \omega^2(n)c_{\mathrm{ww}}(kn; T)\cos(nz)\cos(nz_\ell)\phi_N(z_\ell),$$

and we can compute $(c_{\mathrm{ww}}(k|\partial_z|; T)\phi)_N(z_m)$, $m = 1, 2, \ldots, N$, via an FFT.

Suppose that $T \geqslant 0$ and $k > 0$ are fixed and we take $N = 1024$. We numerically solve

$$-c\phi_N(z_m) + (c_{\mathrm{ww}}(k|\partial_z|; T)\phi)_N(z_m) + \phi_N(z_m)^2 = 0, \quad m = 1, 2, \ldots, N, \tag{20}$$

by means of Newton's method. We parametrically continue the numerical solution over c by means of a pseudo-arclength continuation method [25] (see [22], among others, for nonlinear dispersive equations of the form (7) and (17)), for which the (pseudo-)arclength of a solution branch is the continuation parameter, whereas a parameter continuation method would use c as the continuation parameter and vary it sequentially. The pseudo-arclength continuation method can successfully bypass a turning point of c, at which a parameter continuation method fails because the Jacobian of (20) becomes singular, and Newton's method diverges. See [8] for more discussion.

We say that Newton's method converges if the residual

$$\left(\sum_{m=1}^{N}(-c\phi_N(z_m) + (c_{\mathrm{ww}}(k|\partial_z|; T)\phi)_N(z_m) + \phi_N(z_m)^2)^2\right)^{1/2} \leqslant 10^{-10}$$

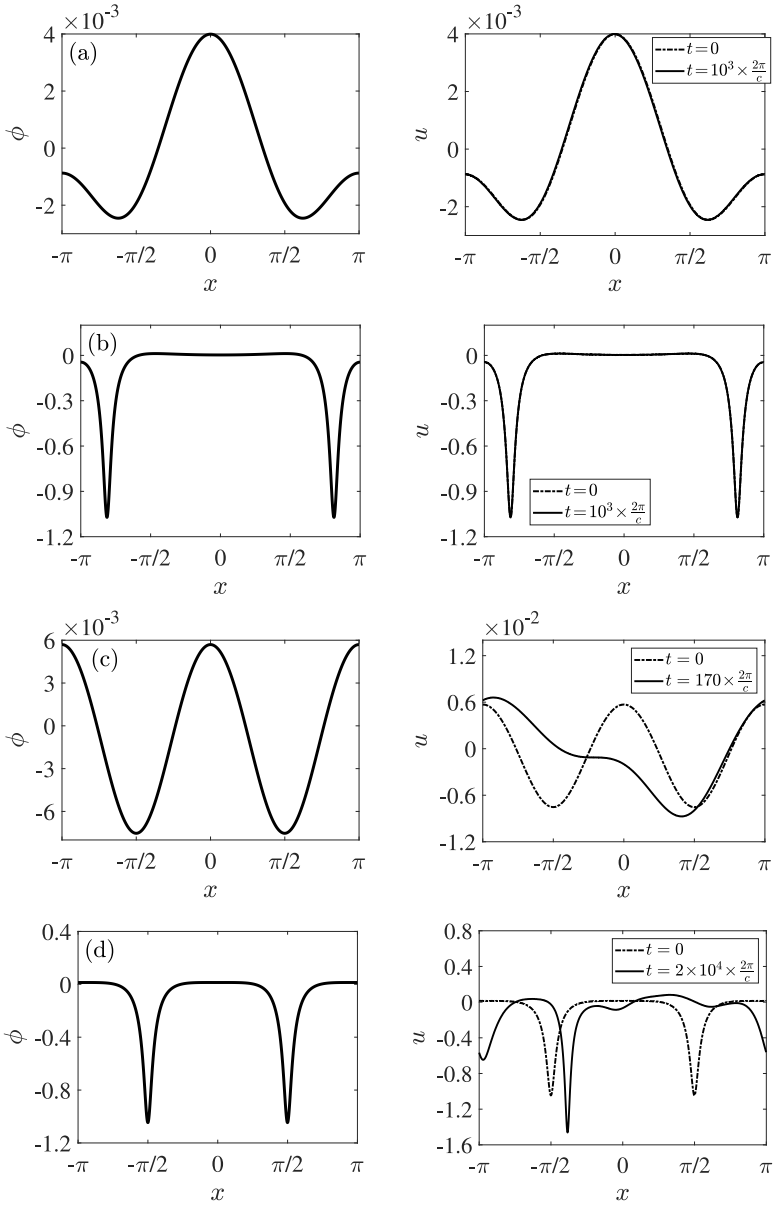

Fig. 6. $T = T(1, 2)$, $k = 1, 2$. Left column: profiles at the points labelled with (a) and (b) ($k = 1$), and (c) and (d) ($k = 2$) in the insets of Fig. 5, for which $c = 0.973$ (a), 0.97 (c), and 0.36 (b,d). Right column: profiles perturbed by small random noise at $t = 0$ (dash-dotted) and of the solutions at later instants of time (solid, see the legends), after translation of the x axis (a,b). Notice different vertical scales.

(see (20)), and this is achieved provided that an initial guess is sufficiently close to a true solution of (8) and (9). To this end, we take a small amplitude cosine function and $c \approx c_{\mathrm{ww}}(k; T)$ as an initial guess for the local bifurcation at $\phi = 0$ and $c = c_{\mathrm{ww}}(k; T)$, or (12) so long as it makes sense. We have also solved (20) using a (Jacobian-free) Newton–Krylov method [26] with absolute and relative tolerance of 10^{-10}. The results correctly match those obtained from Newton's method, corroborating our numerical scheme.

We have run a pseudo-arclength continuation code (see [27], for instance, for the applicability of the code used herein) with a fixed arclength stepsize, to numerically locate and trace solution branches. We have additionally run AUTO [28], a robust numerical continuation and bifurcation software, to corroborate the results. All the results in Section 4 have been obtained by employing AUTO with strict tolerances (`EPSL=1e-12` and `EPSU=1e-12` in the AUTO's constants file). AUTO has the advantage, among many others, of making variable arclength stepsize adaptation (using the option `IADS=1`) and of detecting branch points (using the option `ISP=2` for *all* special points). For the former, provided with minimum

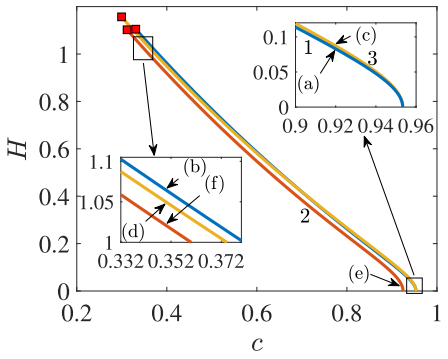

Fig. 7. $T = T(1, 3)$. H vs. c for $k = 1$ (blue), $k = 3$ (yellow), and $k = 2$ (orange). The red squares correspond to the limiting admissible solutions, for which $c \approx 0.3310243764$ ($k = 1$), $c \approx 0.2994866669$ ($k = 3$), and $c \approx 0.3117165220$ ($k = 2$). See Figs. 8 and 9 for the profiles at the points labelled with (a)–(f) in the insets. (For interpretation of the references to colour in this figure legend, the reader is referred to the web version of this article.)

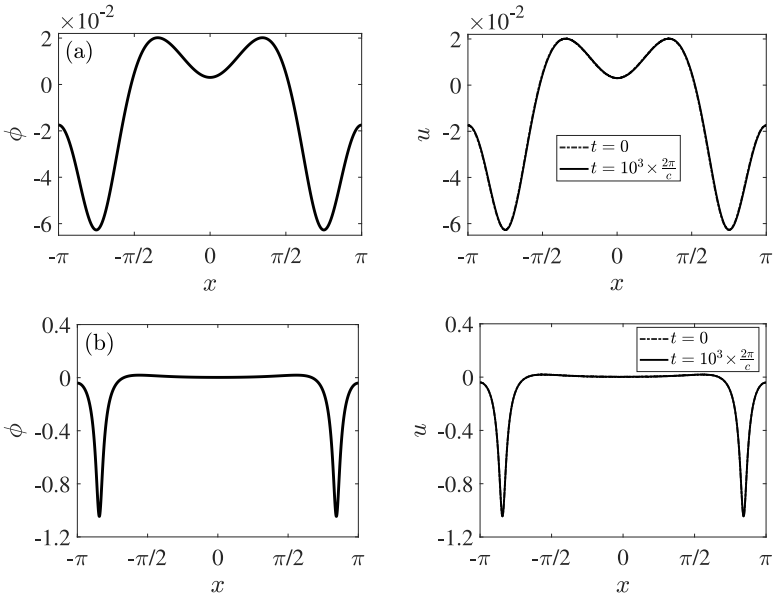

Fig. 8. $T = T(1, 3)$ with $k = 1$. Left column: profiles at the points labelled with (a) and (b) in the insets of Fig. 7, for which $c = 0.92$ and 0.35. Right column: profiles perturbed by small random noise at $t = 0$ (dash-dotted) and of the solutions after 10^3 periods (solid), after translation of the x axis (a).

and maximum allowed absolute values of the pseudo-arclength stepsize, AUTO adjusts the arclength stepsize to be used during the continuation process.

Let ϕ and c numerically approximate a $2\pi/k$ periodic travelling wave of (7), and we turn to numerically experimenting with its (nonlinear) orbital stability and instability. After a 2048-point (full) Fourier spectral discretization of $x \in [-\pi, \pi]$, (7) leads to

$$u_t = \mathbf{L}u + \mathbf{N}(u), \quad \text{where} \quad \mathbf{L} = -c_{\text{ww}}(|\partial_x|; T)\partial_x \quad \text{and} \quad \mathbf{N}(u) = -(u^2)_x, \tag{21}$$

and we numerically solve (21), subject to

$$u(x, 0) = \phi(kx) + 10^{-3} \max_{x\in[-\pi,\pi]} |\phi(kx)|\, U(-1, 1), \tag{22}$$

by means of an integrating factor (IF) method (see [29], for instance, and references therein), where $U(-1, 1)$ is a uniform random distribution. In other words, at the initial time, we perturb ϕ by uniformly distributed random noise of small

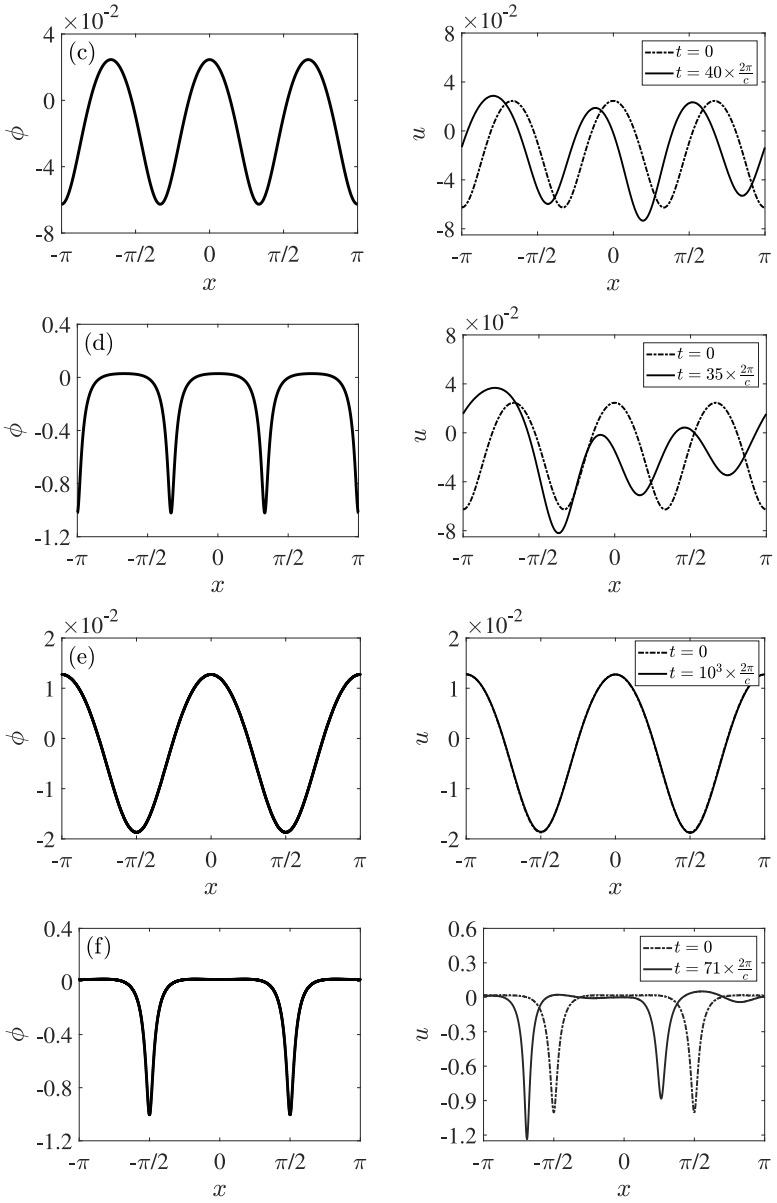

Fig. 9. $T = T(1, 3)$. Similar to Fig. 8 but $k = 3$ (c,d) and $k = 2$ (e,f), $c = 0.92$ (c,e) and 0.35 (d,f). On the right, solid curves are the solution profiles at later times (see the legends), after translation of the x axis (e).

amplitude, depending on the amplitude[4] of ϕ. We pause to remark that the well-posedness for the Cauchy problem of (7) can be rigorously established at least for short time in the usual way by means of a compactness argument.

Following the IF method, let $v = e^{-\mathbf{L}t}u$, so that (21) becomes

$$v_t = e^{-\mathbf{L}t}\mathbf{N}(e^{\mathbf{L}t}v). \tag{23}$$

This ameliorates the stiffness of (21). Notice that (23) is of diagonal form, rather than matrix, in the Fourier space. We advance (23) forward in time by means of a fourth-order four-stage Runge–Kutta (RK4) method [30] with a fixed time stepsize Δt:

$$v_{n+1} = v_n + \frac{\Delta t}{6}\left[a + 2b + 2c + d\right],$$

[4] We treat $\|\phi\|_{L^\infty}$ as the amplitude of ϕ although ϕ is not of mean zero, because the difference is insignificant.

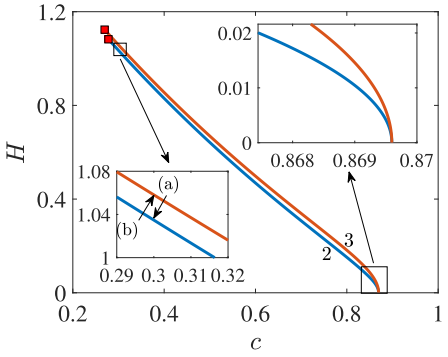

Fig. 10. $T = T(2, 3)$. H vs. c for $k = 2$ (blue) and $k = 3$ (orange). The red squares correspond to the limiting admissible solutions, for which $c \approx 0.27804634505$ ($k = 2$) and $c \approx 0.26958276662$ ($k = 3$). See Fig. 11 for the profiles at the points labelled with (a) and (b) in the inset. (For interpretation of the references to colour in this figure legend, the reader is referred to the web version of this article.)

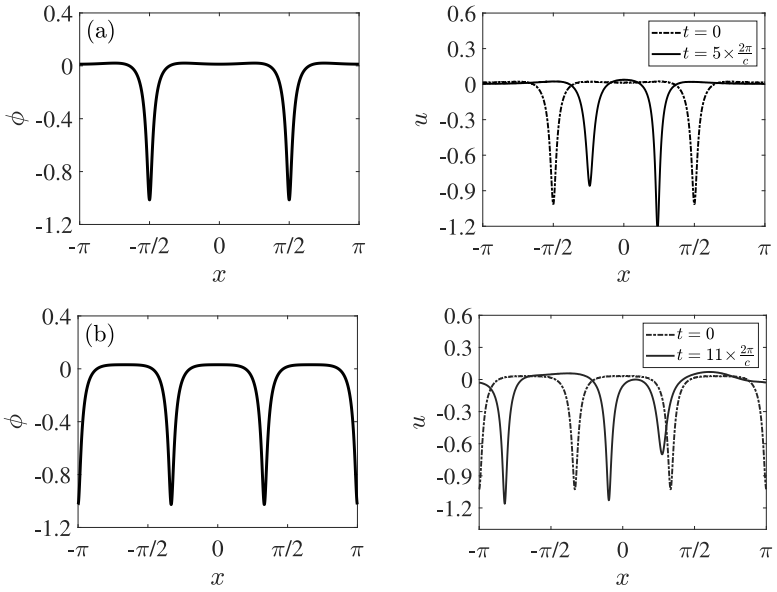

Fig. 11. $T = T(2, 3)$. Left column: profiles at the points labelled with (a) ($k = 2$) and (b) ($k = 3$) in Fig. 10, for which $c = 0.3$. Right column: profiles perturbed by small random noise at $t = 0$ (dash-dotted) and of the solutions at later times (solid, see the legends).

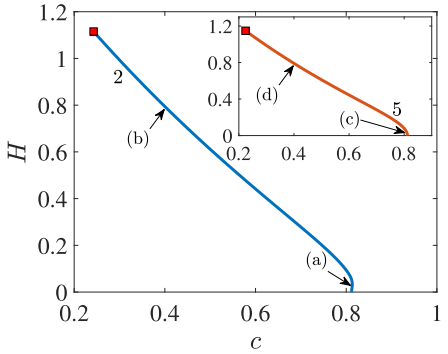

Fig. 12. $T = T(2, 5)$. H vs. c for $k = 2$ (blue) and $k = 5$ (inset, orange). The red squares correspond to the limiting admissible solutions, for which $c \approx 0.24281537129$ ($k = 2$) and $c \approx 0.22417409072$ ($k = 5$). See Figs. 13 and 14 for the profiles at the points labelled with (a)–(d). (For interpretation of the references to colour in this figure legend, the reader is referred to the web version of this article.)

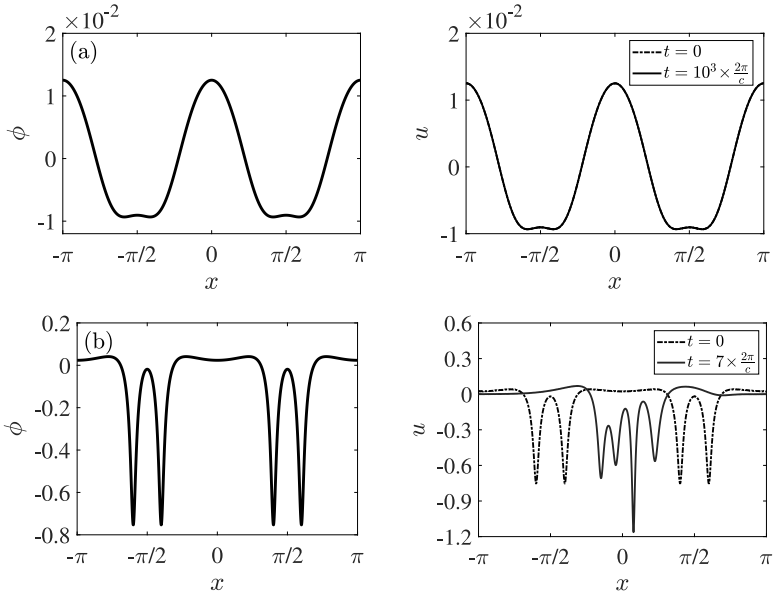

Fig. 13. $T = T(2, 5)$, $k = 2$. Left column: profiles at the points labelled with (a) and (b) in Fig. 12, for which $c = 0.813$ (a) and 0.4 (b). Right column: profiles perturbed by small random noise at $t = 0$ (dash-dotted) and of the solutions at later times (solid), after translation of the x axis (a).

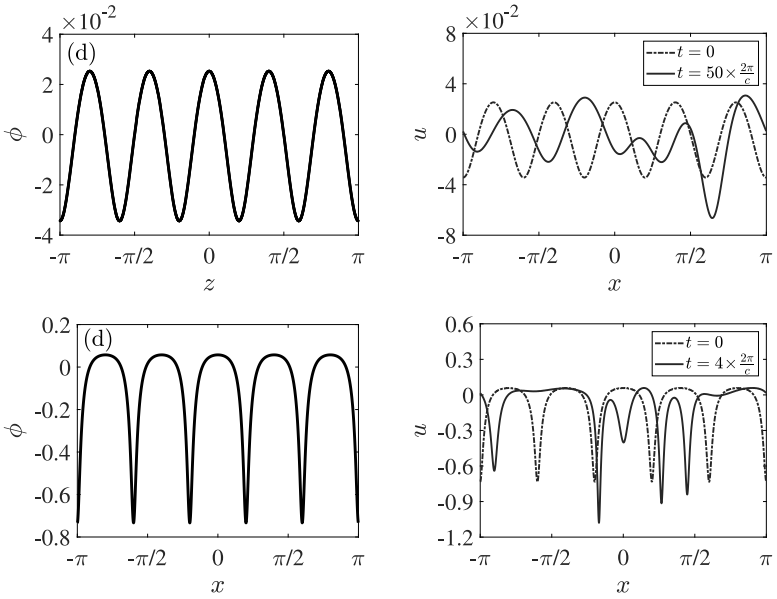

Fig. 14. $T = T(2, 5)$. Similar to Fig. 13 but $k = 5$, $c = 0.805$ (c) and 0.4 (d).

where $v_n = v(t_n)$ and $t_n = n\Delta t$, $n = 0, 1, 2, \ldots$,

$$a = f(v_n, t_n), \qquad b = f(v_n + a/2, t_n + \Delta t/2),$$
$$c = f(v_n + b/2, t_n + \Delta t/2), \qquad d = f(v_n + c, t_n + \Delta t),$$

and $f(v, t) = e^{-\mathbf{L}t}\mathbf{N}(e^{\mathbf{L}t}v)$ (see (23)). We take $\Delta t = 10^{-4} \times 2\pi/c$, where c is the wave speed of ϕ. While such value of Δt ensures numerical stability, some computations, depending on c, require smaller[5] values, for instance, $\Delta t = 10^{-4} \times \pi/c$ or $10^{-5} \times 2\pi/c$. At each time step, we remove aliasing errors by applying the so-called 3/2-rule so that the Fourier coefficients well decay for high frequencies (see [23], for instance).

[5] In most cases, $10^{-4} \times 2\pi/c = O(10^{-4})$ but, for instance, in Fig. 7(b), $c = 0.36$, whence $10^{-4} \times 2\pi/c \approx 0.00174533$, whereas $10^{-5} \times 2\pi/c = O(10^{-4})$.

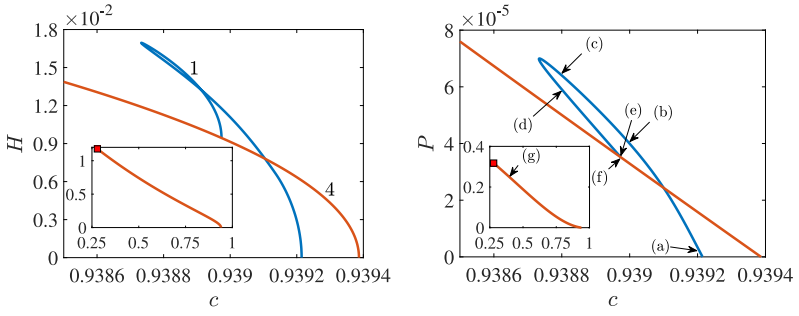

Fig. 15. $T = T(1,4) + 0.0001$. H (left) and P (right) vs. c for $k = 1$ (blue) and $k = 4$ (orange). The red square in the insets corresponds to the limiting admissible solution for $k = 4$, for which $c \approx 0.2788888416$. See Figs. 16–18 for the profiles at the points labelled with (a)–(g) in the right panel. (For interpretation of the references to colour in this figure legend, the reader is referred to the web version of this article.)

We assess the fidelity of our numerical scheme by monitoring (16) for numerical solutions. For unperturbed solutions, $E(t)$, $P(t)$, $M(t)$ have all been conserved to machine precision, whereas for (randomly) perturbed ones, $E(t)$ and $P(t)$ to the order of 10^{-7} and $M(t)$ to machine precision. We have also corroborated our numerical results using two other methods: a higher-order Runge–Kutta method, such as the Runge–Kutta–Fehlberg (RKF) method [30] with time stepsize adaptation and a two-stage (and, thus, fourth-order) Gauss–Legendre implicit[6] Runge–Kutta (IRK4) method [31]. For stable solutions, the results obtained from the RK4 method correctly match those from the RKF and IRK4 methods. However, and for unstable solutions, the instability manifests at slightly different times for the same initial conditions. This is somewhat expected because the local truncation error (LTE) of each method and the convergence error of the IRK4 method act as perturbations. We remark that the RK4 and IRK4 methods have an LTE of the order of $(\Delta t)^4$ whereas the RKF method has $(\Delta t)^6$.

4. Results

We begin by taking $T = 0$ and $k = 1$. Fig. 1 shows the wave height

$$H = \max_{z\in[-\pi,\pi]} \phi(z) - \min_{z\in[-\pi,\pi]} \phi(z) \tag{24}$$

and the momentum

$$P = \frac{1}{2}\int_{-\pi}^{\pi} \phi(z)^2 \, dz \tag{25}$$

from our numerical continuation of 2π periodic and even solutions of (8) and (9). The result agrees, qualitatively, with [22, Figure 4] and others. We find that H monotonically increases to ≈ 0.58156621, highlighted with the red square, for which (13) holds, whereas P increases and then decreases, making one turning point. Also we find that the crest becomes sharper and the trough flatter as H increases. The limiting solution must possess a cusp at the crest [5].

The left column of Fig. 2 shows almost limiting waves. The inset is a close-up near the crest, emphasizing smoothness. The right column shows the profiles of (22), namely periodic travelling waves of (7) perturbed by uniformly distributed random noise of small amplitudes at $t = 0$ (dash-dotted), and of the solutions of (7) at later instants of time (solid). Wave (a), prior to the turning point of P, remains unchanged for 10^3 time periods, after translation of the x axis, implying orbital stability, whereas the inset reveals that wave (b), past the turning point, suffers from crest instability. Indeed, our numerical experiments point to transition from stability to instability at the turning point of P. But there is numerical evidence [32] that waves (a) and (b) are (spectrally) modulationally unstable.

When $T = 4/\pi^2$ and $k = 1$, Fig. 3 shows H and P versus c. Our numerical findings suggest that $H, P \to \infty$ monotonically. Also $\min_{z\in[-\pi,\pi]} \phi(z) \to -\infty$. The solution branch discontinues once (14) holds, highlighted with the red square, though, because the fluid surface would intersect the impermeable bed and, hence, become physically unrealistic. Our numerical continuation works well past the limiting admissible solution, nevertheless. We find that the crest becomes wider and flatter, the trough narrower and more peaked, as H increases. But all solutions must be smooth [11].

The left panel of Fig. 4 shows an example wave. The right panel shows the profiles perturbed by small random noise at $t = 0$ and of the solution of (7) after 10^3 time periods, after translation of the x axis. Our numerical experiments suggest orbital stability for all wave height. But there is numerical evidence of modulational instability when H is large [10].

[6] An implicit method, by construction, enjoys wider regions of absolute stability. This allows us to assess all our results, while avoiding numerical instability that might be observed in explicit methods such as the RK4 and RKF methods. However, the IRK4 method requires a fixed point iteration (in the form of Newton's method) at each time step.

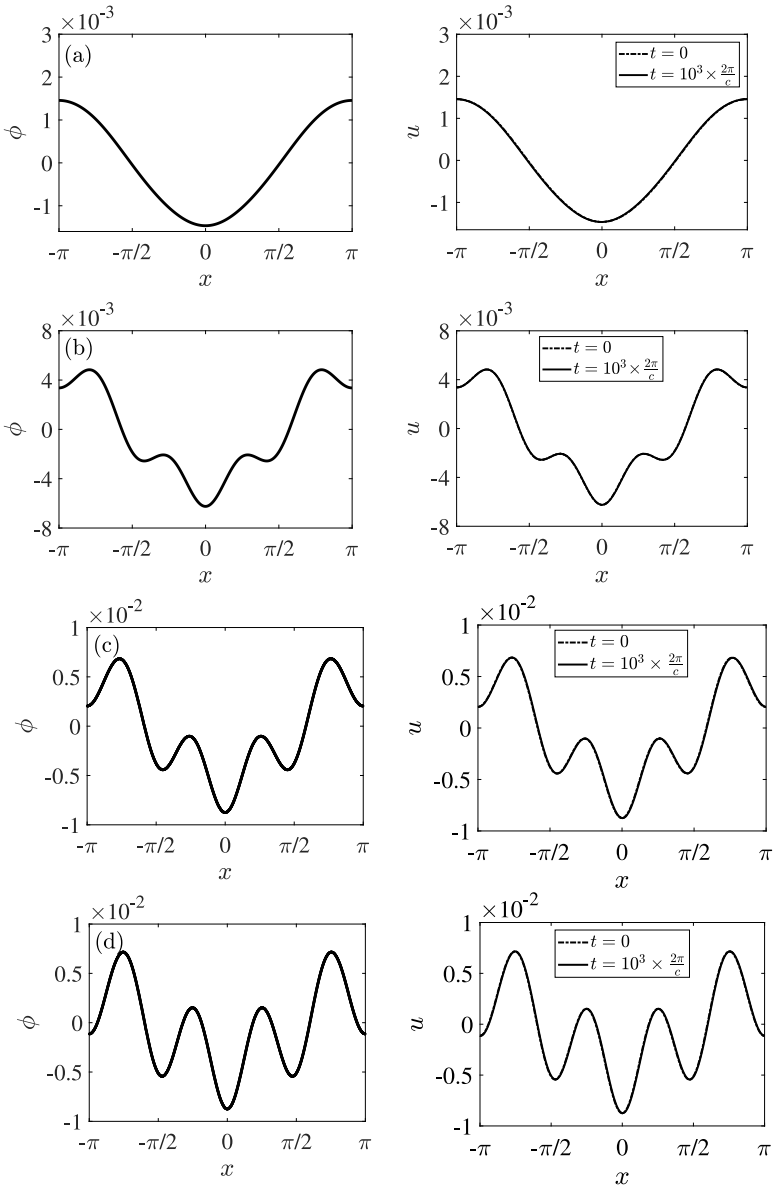

Fig. 16. $T = T(1, 4) + 0.0001$, $k = 1$. Left column: profiles at the points labelled with (a)–(d) in the right panel of Fig. 15, prior to (a) and past (b) crossing the $k = 4$ branch, and prior to (c) and past (d) the turning point of P, for which $c = 0.9392$ (a), 0.939 (b), and 0.9388 (c,d). Right column: profiles perturbed by small random noise at $t = 0$ (dash-dotted) and of the solutions after 10^3 periods (solid), after translation of the x axis.

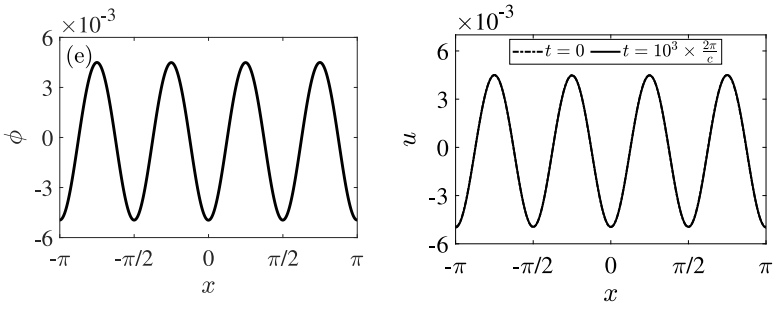

Fig. 17. $T = T(1, 4) + 0.0001$, $k = 1$. Similar to Fig. 16 but almost connecting the $k = 4$ branch, for which $c \approx 0.93897389482$.

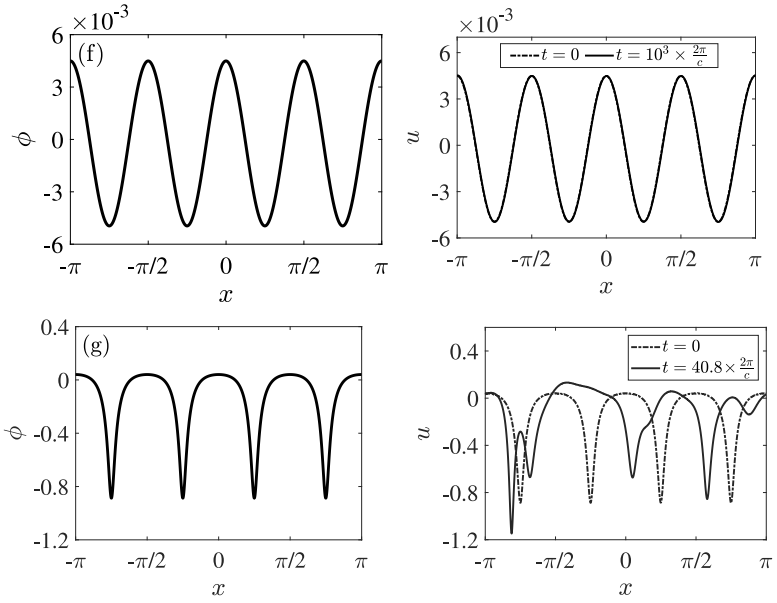

Fig. 18. $T = T(1, 4) + 0.0001$. Similar to Figs. 16 and 17, but $k = 4$, almost connecting the $k = 1$ branch (f) and almost the end of the numerical continuation (g), for which $c \approx 0.93897389482$ (f) and $c = 0.4$ (g).

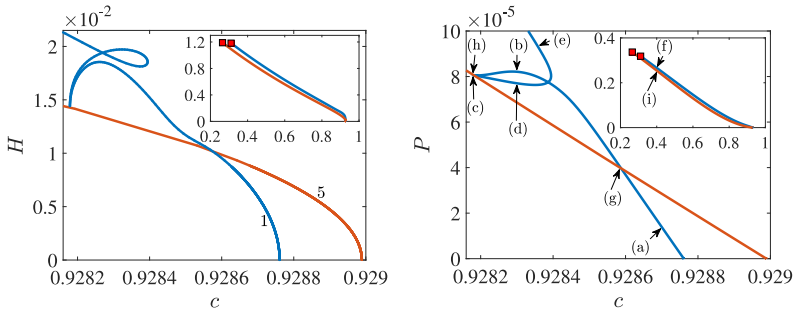

Fig. 19. $T = T(1, 5) + 0.0001$. H and P vs. c for $k = 1$ (blue) and $k = 5$ (orange). The red squares in the insets correspond to the limiting admissible solutions, for which $c \approx 0.3109760939$ ($k = 1$) and $c \approx 0.26500852187$ ($k = 5$). See Figs. 20–22 for the profiles at the points labelled with (a) through (i). (For interpretation of the references to colour in this figure legend, the reader is referred to the web version of this article.)

We turn the attention to $T = T(1, 2) \approx 0.2396825$ (see (10)). There exists a two-parameter sheet of nontrivial, periodic and even solutions of (8) and (9) in the vicinity of $\phi = 0$ and $c = c_{\text{ww}}(1, T) = c_{\text{ww}}(2, T) \approx 0.97166609$ [11]. See also Section 2. Fig. 5 shows H versus c for the $k = 1$ and $k = 2$ branches, all the way up to the limiting admissible solutions. There are no[7] turning points of P. The left column of Fig. 6 shows waves in the $k = 1$ and $k = 2$ branches for small and large H. The small height result agrees with [8, Figure 6].

Observe 'bimodal' waves in the $k = 1$ branch. Indeed, there cannot exist 2π periodic and unimodal waves, whose profile monotonically decreases from a single crest to the trough over the period [11]. See also Section 2. For small wave height, the fundamental mode seems dominant, so that there is one crest over the period $= 2\pi$, but the fundamental and second modes are resonant, whereby a much smaller wave breaks up the trough into two. See the left panel of Fig. 6(a). As H increases, the effects of the second mode seem more pronounced, so that the wave separating the troughs becomes higher. See the left of Fig. 6(b). Observe on the other hand π periodic and unimodal waves in the $k = 2$ branch. See the left of Fig. 6(c,d). We find that the crests become wider and flatter, the troughs narrower and more peaked, as H increases in the $k = 1$ and $k = 2$ branches. See the left of Fig. 6(b,d).

Our numerical experiments suggest orbital stability for the $k = 1$ branch (see the right panels of Fig. 6(a,b)) versus instability for $k = 2$ (see the right of Fig. 6(c,d)).

We take matters further to $T = T(1, 3)$. See Figs. 7–9. The results for the $k = 1$ and $k = 3$ branches are similar to those when $T = T(1, 2)$ and $k = 1, 2$. We pause to remark that in the $k = 1$ branch, for small H, a smaller wave breaks up the

[7] We observe a turning point of P for greater wave height, but the solution is inadmissible.

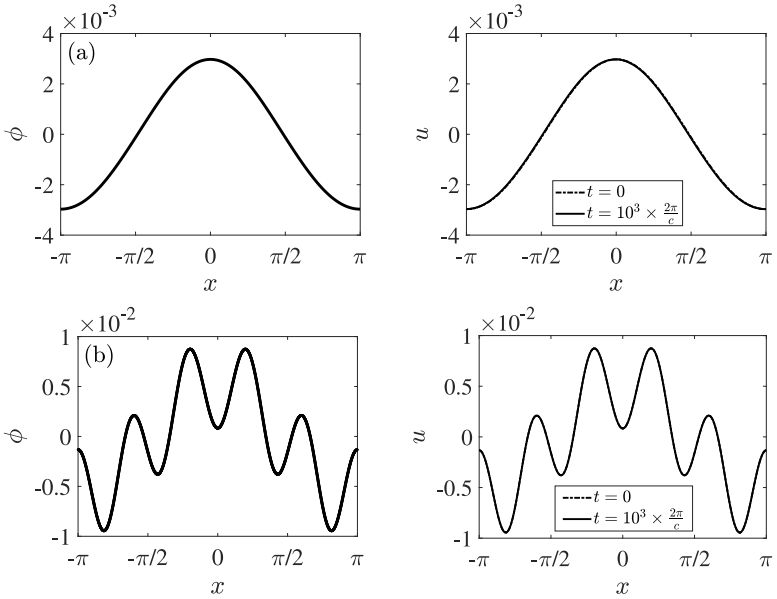

Fig. 20. $T = T(1, 5) + 0.0001$, $k = 1$. Left column: profiles at the points labelled with (a) and (b) in the right panel of Fig. 19, prior to (a) and past (b) crossing the $k = 5$ branch, for which $c = 0.9287$ (a) and 0.9283 (b). Right column: profiles perturbed by small random noise at $t = 0$ (dash-dotted) and of the solutions after 10^3 periods (solid), after translation of the x axis (a).

trough into two, and a much smaller wave breaks up the crest into two. See the left panel of Fig. 8(a). As H increases, the wave separating the crests becomes lower, transforming into one wide and flat crest, whereas the wave separating the troughs become higher (see the left of Fig. 8(b)), resembling those when $T = T(1, 2)$ and $k = 1$. Observe π periodic and unimodal waves in the $k = 2$ branch, orbitally stable for small H versus unstable for large H. See Fig. 9(e,f).

When $T = T(2, 3)$, we find π and $2\pi/3$ periodic unimodal waves in the $k = 2$ and $k = 3$ branches, respectively, corroborating a local bifurcation theorem [11]. See also Fig. 10 and Section 2. We find that the crests become wider and flatter, the troughs narrower and more peaked, as H increases. See the left column of Fig. 11. Our numerical experiments (see the right of Fig. 11) suggest orbital instability for the $k = 2$ branch for large H and for $k = 3$ for all H.

When $T = T(2, 5)$, on the other hand, the left column of Fig. 13 shows bimodal waves in the $k = 2$ branch. The local bifurcation theorem [11] dictates π periodic and unimodal waves, but we numerically find that they are not in the $k = 2$ branch. For small H, for instance, for wave (a), a smaller wave breaks up the trough into two over the half period. For greater H, for instance, for wave (b), the troughs become narrower and more peaked. Our numerical experiments (see the right of Figs. 13 and 14) suggest orbital stability for the $k = 2$ branch for small H versus instability for $k = 2$ for large H and for $k = 5$ for all H.

To proceed, when $T = T(1, 4)$, the $k = 1$ branch lies above and to the right of the $k = 4$ branch at least for small H (not shown), but as T increases, $c_{\mathrm{ww}}(4; T)$ increases more rapidly than $c_{\mathrm{ww}}(1; T)$, so that when $T = T(1, 4) + 0.001$, for instance, the $k = 1$ branch crosses the $k = 4$ branch. Fig. 15 shows H and P versus c in the $k = 1$ and $k = 4$ branches for all admissible solutions. The small height result agrees with [8, Figure 10(a)]. We find that in the $k = 1$ branch, H and P turn to connect the $k = 4$ branch, whereas in the $k = 4$ branch, H and P monotonically increase to the limiting admissible solution, highlighted by the red square in the insets.

The left panels of Figs. 16–18 show several profiles along the $k = 1$ and $k = 4$ branches. In the $k = 1$ branch, for small H, wave (a), for instance, is 2π periodic and unimodal. After the $k = 1$ branch crosses the $k = 4$ branch, on the other hand, wave (b), for instance, becomes multi-modal, resembling those when $T = T(1, 4)$ and $k = 1$. Continuing along the $k = 1$ branch, for waves (c) and (d), for instance, high frequency ripples of $k = 4$ ride a carrier wave of $k = 1$. When the $k = 1$ and $k = 4$ branches almost connect, wave (e) in the $k = 1$ branch and wave (f) for $k = 4$ are almost the same. In the $k = 4$ branch, wave (g), for instance, is $\pi/2$ periodic and unimodal.

Our numerical experiments (see the right panels of Figs. 16–18) suggest orbital stability for the $k = 1$ branch for all H and for $k = 4$ for small H, versus instability for $k = 4$ for large H. Particularly, stability and instability do not change at the turning point of P.

Last but not least, when $T = T(1, 5) + 0.0001$, Fig. 19 shows H and P versus c for the $k = 1$ and $k = 5$ branches. The small height result agrees with [8, Figure 10(b)]. We find that the $k = 1$ branch crosses and connects the $k = 5$ branch, like when $T = T(1, 4) + 0.0001$ and $k = 1, 4$, but it continues after connecting all the wave up to the limiting admissible solution. See the insets. The left panels of Figs. 20–22 show several profiles along the $k = 1$ and $k = 5$ branches. The results for the $k = 1$ branch up to connecting and for $k = 5$ are similar to those when $T = T(1, 4) + 0.0001$ and $k = 1, 4$.

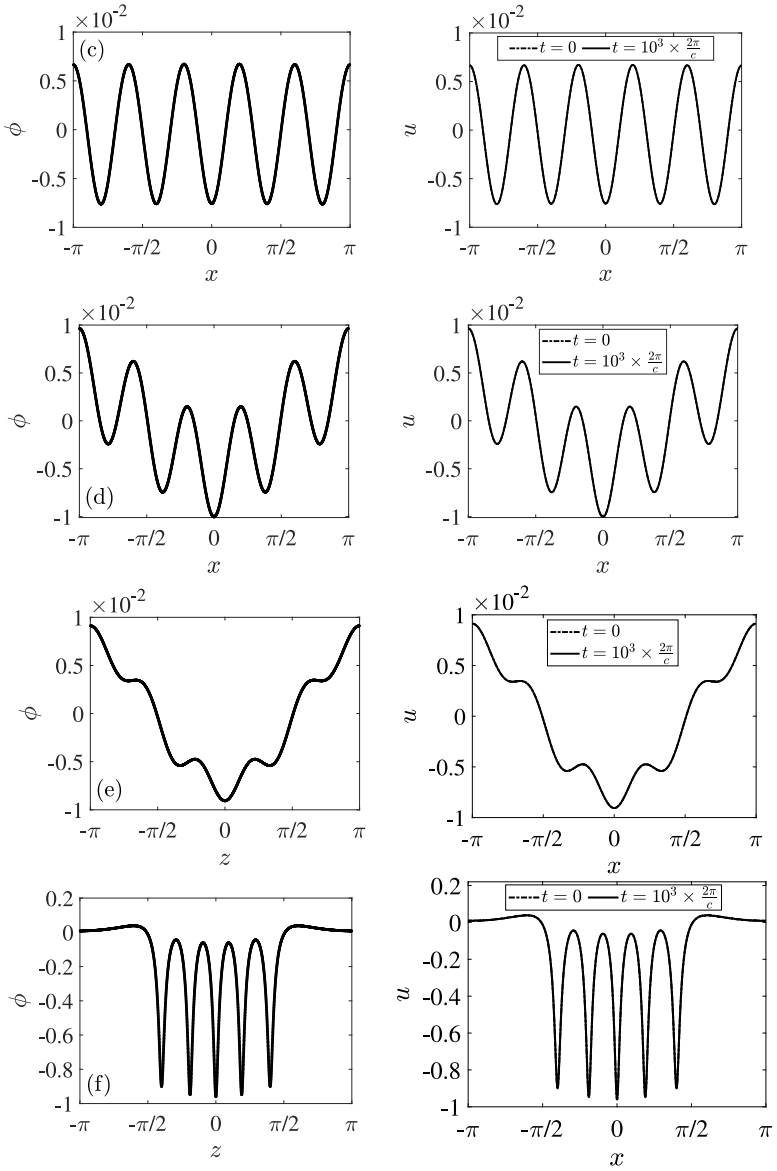

Fig. 21. $T = T(1, 5) + 0.0001$, $k = 1$. Similar to Fig. 20, almost connecting the $k = 5$ branch (c), prior to (d) and past (e) crossing the $k = 1$ branch itself, and almost the end of the numerical continuation (f), for which $c = 0.92817880141$ (c), 0.9283 (d), 0.92836 (e), and 0.4 (f).

In the $k = 1$ branch, after it connects the $k = 4$ branch at the point (c), the results are similar to those when $T = T(1, 5)$ and $k = 1$. See waves (d), (e) and (f). Our numerical experiments (see the right panels of Figs. 20–22) suggest orbital stability for the $k = 1$ branch for all H and for $k = 5$ for small H, versus instability for $k = 5$ for large H.

We emphasize orbital stability for the $k = 1$ branch for all $T > 0$ for all wave height throughout our numerical experiments.

5. Discussion

Here we employ efficient and highly accurate numerical methods for computing periodic travelling waves of (7) and experimenting with their (nonlinear) orbital stability and instability. Our findings suggest, among many others, stability whenever $T > 0$ for the $k = 1$ branch versus instability when $0 < T < 1/3$ for the $k \geqslant 2, \in \mathbb{N}$ branches at least for great wave height. Currently under investigation [33] is to numerically investigate (spectral) modulational stability and instability of orbitally stable waves. It will be interesting to take matters further to all $T \geqslant 0$ to all k, to classify the stability and instability of all periodic travelling waves. Also it will be interesting to devise other numerical continuation

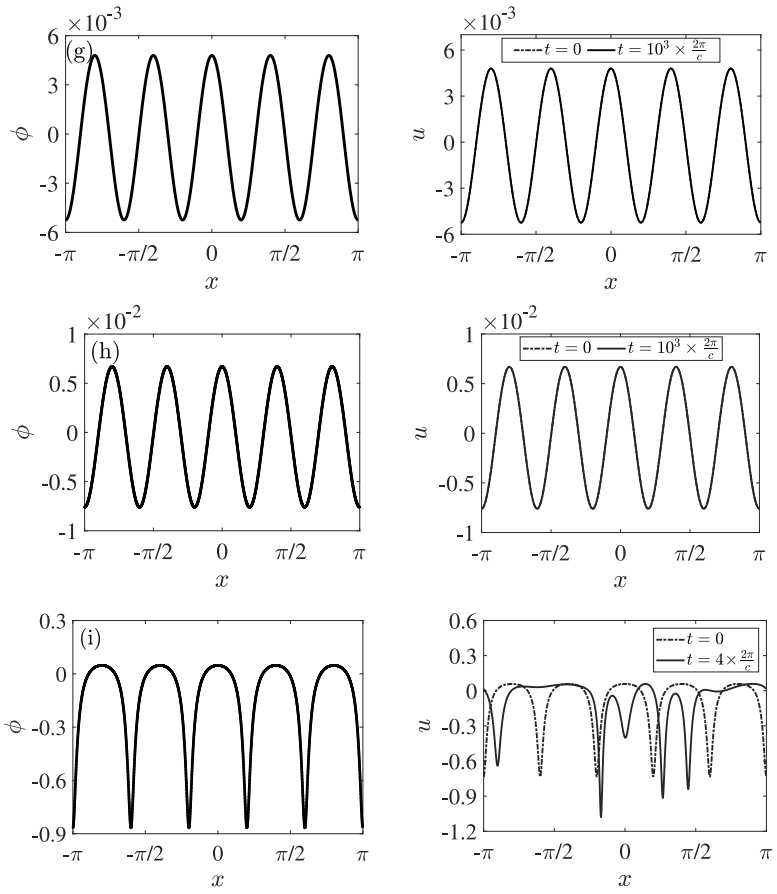

Fig. 22. $T = T(1, 5) + 0.0001$, $k = 5$. Left column: profiles at the points labelled with (g)–(i) in the right panel of Fig. 20, almost crossing the $k = 1$ branch (g), almost connecting the $k = 1$ branch (h), and almost the end of the numerical continuation (i), for which $c = 0.9285878$ (g), 0.92817880141 (h), and 0.4 (i). Right column: profiles perturbed by small random noise at $t = 0$ (dash-dotted) and of the solutions at later times (solid).

methods, for instance, deflated continuation techniques [34,35], for detecting *disconnected* solution branches and others. Our methodology will be useful for exploring the nonlinear dynamics of modulationally unstable waves. Also it can help tackle the capillary–gravity wave problem and other nonlinear dispersive equations, for instance, the full-dispersion Camassa–Holm equation [13] and the Whitham equation for waves in a thin elastic sheet at the surface of a fluid [36]. Of course, it is of great importance to rigorously prove the numerical results, particularly, orbital stability. The proof for (17) [21] (see also [20] for solitary waves) make strong use of special properties of the fractional Laplacian, and it is far from being trivial what to do more generally.

Declaration of competing interest

The authors declare that they have no known competing financial interests or personal relationships that could have appeared to influence the work reported in this paper.

Acknowledgements

The authors are grateful to Henrik Kalisch for helpful discussions. EGC acknowledges the hospitality of the Department of Mathematics at the University of Illinois at Urbana-Champaign where early stages of this work took place.

References

[1] G.B. Whitham, Variational methods and applications to water waves, Proc. R. Soc. Lond. A 299 (1456) (1967) 6–25.
[2] G.B. Whitham, Linear and Nonlinear Waves, in: Pure and Applied Mathematics (New York), John Wiley & Sons, Inc., New York, 1999, p. xviii+636, Reprint of the 1974 original, A Wiley-Interscience Publication..

[3] Daulet Moldabayev, Henrik Kalisch, Denys Dutykh, The Whitham equation as a model for surface water waves, Physica D 309 (2015) 99–107.
[4] Vera Mikyoung Hur, Wave breaking in the Whitham equation, Adv. Math. 317 (2017) 410–437.
[5] Mats Ehrnström, Erik Wahlén, On Whitham's conjecture of a highest cusped wave for a nonlocal dispersive equation, Ann. Inst. H. Poincaré Anal. Non Linéaire 36 (6) (2019) 1603–1637.
[6] Vera Mikyoung Hur, Mathew A. Johnson, Modulational instability in the Whitham equation for water waves, Stud. Appl. Math. 134 (1) (2015) 120–143.
[7] Vera Mikyoung Hur, Mathew A. Johnson, Modulational instability in the Whitham equation with surface tension and vorticity, Nonlinear Anal. 129 (2015) 104–118.
[8] Filippo Remonato, Henrik Kalisch, Numerical bifurcation for the capillary Whitham equation, Physica D 343 (2017) 51–62.
[9] Evgueni Dinvay, Daulet Moldabayev, Denys Dutykh, Henrik Kalisch, The Whitham equation with surface tension, Nonlinear Dynam. 88 (2) (2017) 1125–1138.
[10] John D Carter, Morgan Rozman, Stability of periodic, traveling-wave solutions to the capillary Whitham equation, Fluids 4 (1) (2019) 58.
[11] Mats Ehrnström, Mathew A. Johnson, Ola I.H. Maehlen, Filippo Remonato, On the bifurcation diagram of the capillary-gravity Whitham equation, Water Waves 1 (2) (2019) 275–313.
[12] Vera Mikyoung Hur, Ashish Kumar Pandey, Modulational instability in a full-dispersion shallow water model, Stud. Appl. Math. 142 (1) (2019) 3–47.
[13] Vera Mikyoung Hur, Ashish Kumar Pandey, Modulational instability in the full-dispersion Camassa–Holm equation, Proc. A. 473 (2203) (2017) 20171053, 18.
[14] Vera Mikyoung Hur, Shallow water models with constant vorticity, Eur. J. Mech. B Fluids 73 (2019) 170–179.
[15] Ashish Kumar Pandey, The effects of surface tension on modulational instability in full-dispersion water-wave models, Eur. J. Mech. B Fluids 77 (2019) 177–182.
[16] Henrik Kalisch, Didier Pilod, On the local well-posedness for a full-dispersion Boussinesq system with surface tension, Proc. Amer. Math. Soc. 147 (6) (2019) 2545–2559.
[17] J.F. Toland, M.C.W. Jones, The bifurcation and secondary bifurcation of capillary-gravity waves, Proc. R. Soc. Lond. Ser. A Math. Phys. Eng. Sci. 399 (1817) (1985) 391–417.
[18] Mark Jones, John Toland, Symmetry and the bifurcation of capillary-gravity waves, Arch. Ration. Mech. Anal. 96 (1) (1986) 29–53.
[19] P.J. Aston, Local and global aspects of the $(1, n)$ mode interaction for capillary-gravity waves, Physica D 52 (2–3) (1991) 415–428.
[20] Felipe Linares, Didier Pilod, Jean-Claude Saut, Remarks on the orbital stability of ground state solutions of fKdV and related equations, Adv. Differential Equations 20 (9–10) (2015) 835–858.
[21] Vera Mikyoung Hur, Mathew A. Johnson, Stability of periodic traveling waves for nonlinear dispersive equations, SIAM J. Math. Anal. 47 (5) (2015) 3528–3554, MR 3397429.
[22] Henrik Kalisch, Daulet Moldabayev, Olivier Verdier, A numerical study of nonlinear dispersive wave models with SpecTraVVave, Electron. J. Differential Equations (2017) Paper No. 62, 23.
[23] John P. Boyd, Chebyshev and Fourier Spectral Methods, second ed., Dover Publications, Inc., Mineola, NY, 2001, p. xvi+668.
[24] David Gottlieb, Steven A. Orszag, Numerical Analysis of Spectral Methods: Theory and Applications, in: CBMS-NSF Regional Conference Series in Applied Mathematics, vol. 26, Society for Industrial and Applied Mathematics, Philadelphia, Pa., 1977, p. v+172.
[25] Eusebius Doedel, Laurette S. Tuckerman (Eds.), Numerical methods for bifurcation problems and large-scale dynamical systems, in: Proceedings of the Workshop on Numerical Methods for Bifurcation Problems Held September 15–19, 1997 and the Workshop on Large Scale Dynamical Systems Held September 29–OCtober 3, 1997 in Minneapolis, MN, in: The IMA Volumes in Mathematics and its Applications, vol. 119, Springer-Verlag, New York, 2000, p. x+471.
[26] C.T. Kelley, Solving Nonlinear Equations with Newton's Method, in: Fundamentals of Algorithms, vol. 1, Society for Industrial and Applied Mathematics (SIAM), Philadelphia, PA, 2003, p. xiv+104.
[27] J. Sullivan, E.G. Charalampidis, J. Cuevas-Maraver, P.G. Kevrekidis, N.I. Karachalios, Kuznetsov–Ma breather-like solutions in the Salerno model, Eur. Phys. J. Plus 135 (7) (2020) 607.
[28] Eusebius Doedel, AUTO, http://indy.cs.concordia.ca/auto/.
[29] Aly-Khan Kassam, Lloyd N. Trefethen, Fourth-order time-stepping for stiff PDEs, SIAM J. Sci. Comput. 26 (4) (2005) 1214–1233.
[30] E. Hairer, S.P. Nørsett, G. Wanner, Solving Ordinary Differential Equations. I, second ed., in: Springer Series in Computational Mathematics, vol. 8, Springer-Verlag, Berlin, 1993, p. xvi+528, Nonstiff problems.
[31] E. Hairer, G. Wanner, Solving Ordinary Differential Equations. II, second ed., in: Springer Series in Computational Mathematics, vol. 14, Springer-Verlag, Berlin, 1996, p. xvi+614, http://dx.doi.org/10.1007/978-3-642-05221-7, Stiff and differential-algebraic problems.
[32] Nathan Sanford, Keri Kodama, John D. Carter, Henrik Kalisch, Stability of traveling wave solutions to the Whitham equation, Phys. Lett. A 378 (30–31) (2014) 2100–2107.
[33] Jonh D. Carter, Efstathios G. Charalampidis, Vera Mikyoung Hur, A numerical study of spectral stability for the capillary-gravity Whitham equation, 2021, in preparation.
[34] N. Boullé, E.G. Charalampidis, P.E. Farrell, P.G. Kevrekidis, Deflation-based identification of nonlinear excitations of the three-dimensional Gross-Pitaevskii equation, Phys. Rev. A 102 (5) (2020) 053307, 8 pp.– 53314.
[35] E.G. Charalampidis, N. Boullé, P.E. Farrell, P.G. Kevrekidis, Bifurcation analysis of stationary solutions of two-dimensional coupled Gross-Pitaevskii equations using deflated continuation, Commun. Nonlinear Sci. Numer. Simul. 87 (2020) 105255, 24.
[36] Evgueni Dinvay, Henrik Kalisch, Daulet Moldabayev, Emilian I. Părău, The Whitham equation for hydroelastic waves, Appl. Ocean Res. 89 (2019) 202–210.